Aneurysm Pose Estimation with Deep Learning

Youssef Assis, Liang Liao, Fabien Pierre, René Anxionnat, Erwan Kerrien

▶ **To cite this version:**

Youssef Assis, Liang Liao, Fabien Pierre, René Anxionnat, Erwan Kerrien. Aneurysm Pose Estimation with Deep Learning. Medical Image Computing and Computer Assisted Intervention (MICCAI), Oct 2023, Vancouver, Canada. 10.1007/978-3-031-43895-0_51 . hal-04207337

HAL Id: hal-04207337

https://hal.univ-lorraine.fr/hal-04207337v1

Submitted on 15 Oct 2023

HAL is a multi-disciplinary open access archive for the deposit and dissemination of scientific research documents, whether they are published or not. The documents may come from teaching and research institutions in France or abroad, or from public or private research centers.

L'archive ouverte pluridisciplinaire **HAL**, est destinée au dépôt et à la diffusion de documents scientifiques de niveau recherche, publiés ou non, émanant des établissements d'enseignement et de recherche français ou étrangers, des laboratoires publics ou privés.

Aneurysm Pose Estimation with Deep Learning

Youssef Assis[1], Liang Liao[1,2,3], Fabien Pierre[1], René Anxionnat[2,3], and Erwan Kerrien[1]

[1] Université de Lorraine, CNRS, Inria, LORIA, F-54000 Nancy, France
[2] Université de Lorraine, CHRU-Nancy, Department of Diagnostic and Therapeutic Interventional Neuroradiology, F-54000 Nancy, France
[3] Université de Lorraine, Inserm, IADI, F-54000 Nancy, France

Note: This preprint has not undergone peer review (when applicable) or any post-submission improvements or corrections. The Version of Record of this contribution is published in "Medical Image Computing and Computer Assisted Intervention – MICCAI 2023", and is available online at `https://doi.org/10.1007/978-3-031-43895-0_51`.

Abstract. The diagnosis of unruptured intracranial aneurysms from time-of-flight Magnetic Resonance Angiography (TOF-MRA) images is a challenging clinical problem that is extremely difficult to automate. We propose to go beyond the mere detection of each aneurysm and also estimate its size and the orientation of its main axis for an immediate visualization in appropriate reformatted cut planes. To address this issue, and inspired by the idea behind YOLO architecture, a novel one-stage deep learning approach is described to simultaneously estimate the localization, size and orientation of each aneurysm in 3D images. It combines fast and approximate annotation, data sampling and generation to tackle the class imbalance problem, and a cosine similarity loss to optimize the orientation. We evaluate our approach on two large datasets containing 416 patients with 317 aneurysms using a 5-fold cross-validation scheme. Our method achieves a median localization error of 0.48 mm and a median 3D orientation error of 12.27 degrees, demonstrating an accurate localization of aneurysms and an orientation estimation that comply with clinical practice. Further evaluation is performed in a more classical detection setting to compare with state-of-the-art nnDetecton and nnUNet methods. Competitive performance is reported with an average precision of 76.60%, a sensitivity score of 82.93%, and 0.44 false positives per case. Code and annotations are publicly available at `https://gitlab.inria.fr/yassis/DeepAnePose`.

Keywords: Pose Estimation · Object Detection · Intracranial Aneurysms

1 Introduction

Intracranial aneurysms are abnormal focal dilations of cerebral blood vessels. Their rupturing accounts for 85% of Subarachnoid Hemorrhages (SAH), and is

associated with high morbidity and mortality rates [23]. Early detection and monitoring of Unruptured Intracranial Aneurysms (UIA) has become a problem of increasing clinical importance. Due to its non-invasive nature, 3D time-of-flight Magnetic Resonance Angiography (TOF-MRA) is the most suitable imaging technique for screening. However, detecting aneurysms in TOF-MRA volumes is a costly process that requires radiologists to scroll through different cut planes [7]. Therefore, an automated method to detect aneurysms and provide immediate appropriate visualization would be a valuable tool to assist radiologists in their clinical routine. We envision a dynamic browsing of cut planes rotating around the main axis of the aneurysm to facilitate the analysis of the aneurysm and the surrounding angioarchitecture. This requires estimating the location and orientation, i.e. the pose, of the aneurysm. This pose has been related to the risk of rupture [13] and could also be used for image registration [17].

Automated methods for detecting UIAs range from traditional Computer-Aided Detection (CAD) systems using image filtering techniques [1,27], to advanced deep learning methods based on Convolutional Neural Networks (CNNs). Although 2D and 2.5D methods have been proposed [19,24,26], most recent methods are fully 3D patch-based approaches. In 2020, the Aneurysm Detection and SegMentation (ADAM) challenge [25] compared various detection methods using TOF-MRA data. The class imbalance problem caused by the scarcity of aneurysm voxels inside an image volume, was addressed through loss functions and/or data augmentation. The top-performing method was nnDetection [3], which relies on a 3D bounding box representation. nnUNet [9], ranked third, uses the UNet [6] semantic segmentation architecture. Both methods consider large patches as input, which requires significant computing power and large databases for reliable sample modeling. Detection provides localization, but aneurysm orientation is challenging to estimate, due to the noise/artifacts in medical images, annotation burden, with inter- and intra-observer variability, and small size and shape diversity which imply more uncertainty than for larger objects.

Estimating the pose of organs has been investigated in the literature as a slice positioning problem. A set of slices must be optimally selected relative to the pose of the knee [5,14,28,29], shoulder [29], or brain [4,12,10]. These organs are single instances of large objects with specific shapes, standard positions and orientations within the images. On the contrary, aneurysms are very small pathologies with unspecific shapes, undefined locations and numbers. These algorithms can be categorized into registration-based and learning-based methods. Registration-based methods [5,12] rely on rigid transformations, which limits their application to (quasi-)rigid body parts. Learning-based methods [10,20,28,29] typically consist of a two-stage pipeline. The first stage detects the Regions-of-Interest (ROIs), while the second stage regresses/estimates the object orientation for each ROI. For instance, faster-RCNN [22] and V-Net [18] architectures were employed in [29] to localize and segment the orientation plane, defined by a center location and two unit vectors. However, existing methods are mainly intended for low-resolution images like MR scout scans, and their computational demands increase with high-resolution images. One-stage approaches, such as YOLO [21],

demonstrate promising performance in object detection with greater flexibility than two-stage approaches.

In this paper, we introduce a novel one-stage method to simultaneously localize, and estimate the size and the orientation of aneurysms from 3D TOF-MRA images. A fast and approximate annotation is used. To address the class imbalance problem, a small patch approach is combined with dedicated data sampling and generation strategies. We follow a landmark approach to estimate the aneurysm pose, while avoiding rotation discontinuity problems associated with Euler angles and quaternions [30]. Furthermore, we propose a 3D extension of YOLO architecture, using a cosine similarity loss for the orientation.

2 Materiels and methods

2.1 Datasets and data annotation

In this work, two TOF-MRA aneurysm datasets were used. The first dataset includes 132 exams (75 female, 57 male) collected at our medical institution between 2015 and 2021 according to the following inclusion criteria: diagnosed unruptured saccular aneurysms smaller than 20mm, no pre-treated aneurysm or fusiform aneurysm. A single exam was included per patient (i.e. no follow-up exams). All images were acquired using a 3T scanner (GE Discovery MR750w). Acquisition parameters included TR=28ms, TE=3.4ms, slice thickness=0.8mm, and 4 slabs (54 slices/slab), resulting in $512 \times 512 \times 254$ volumes with a $0.47 \times 0.47 \times 0.4\text{mm}^3$ voxel size. Each DICOM data was anonymized on the clinical site before processing. As per the charter of our university hospital, the anonymous use of imaging data acquired in clinical practice is authorized for research purposes, in accordance with the principle of non-opposition of the patient. Each image contained from one (84/132) to five aneurysms (4 subjects), totaling 206 aneurysms with a mean diameter of 3.97±2.32mm (range: 0.96-19.63mm). Most aneurysms were small, with 81 below 3mm and 77 between 3-5mm.

The second dataset is the public aneurysm dataset [7], which comprises 412 images. After applying the same inclusion criteria as the in-house dataset, 270 images were selected for analysis. Two expert neuroradiologists reviewed the dataset, identifying 7 additional aneurysms and removing 5 aneurysms as they were simple irregularities on the vessel surface. The resulting images contains 164 aneurysms with similar statistics to the first dataset: mean diameter of 3.74±2.17mm (range: 1.37-13.64mm), 66 below 3mm and 72 between 3-5mm. Each image contained from 0 (130 healthy subjects) to 3 (3 subjects) aneurysms.

Previous works on aneurysm detection and segmentation relied on voxel-wise labeling, which is time-consuming and susceptible to intra- and inter-rater variability. To address these limitations, weak annotations using spheres have been recently investigated [2,7]. Similar to [2], our annotation involves labeling each aneurysm using two points: the center of the neck (i.e. ostium) and another point along its main axis (i.e. dome). This method provides information about aneurysms location, size, and their orientation (see Fig. 1). To simplify the placement of the two points in the volume rendering view, we developed a Python

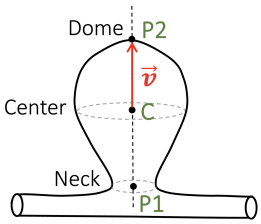

Fig. 1: Fast aneurysm annotation: 2 points ($P1$, $P2$) define a sphere. The ground truth pose is inferred as the center $C = (P1+P2)/2$ and axis vector $\vec{v} = P2-C$.

extension for the 3D Slicer software [8], which provides a real-time visualization of the sphere in the canonical cut planes.

2.2 Data sampling and generation

Accurate modeling of aneurysm and background properties is crucial for pose estimation tasks. We use small $96 \times 96 \times 96$ voxel patches with an isotropic voxel size of 0.4mm, resulting in 38.4mm side length patches. This approach is computationally efficient compared to larger patch methods, such as nnDetection [3] and nnUNet [9]. It also allows for the extraction of multiple non-intersecting negative (aneurysm-free) patches from each image for more training data and reliable background modeling. However, this approach introduces a class imbalance problem, as there is only a single positive patch for each aneurysm. To overcome this, we used adapted data sampling strategies. Our first strategy duplicates each positive patch 50 times and applies random distortions at each epoch to synthesize a variety of aneurysm shapes: each control point on a $3 \times 3 \times 3$ lattice enclosing the patch, except the central point, is moved randomly by 3 mm in all 3 space directions, and the distortion field is interpolated using cubic spline interpolation. To guide the model to discriminate between healthy vessels and aneurysms, our second strategy pre-selects 40 non-intersecting negative patches per image, 30 of which are centered on blood vessels by iteratively choosing the brightest voxels as patch centers. Each training epoch used a set composed of all positive patches, completed with random negative patches equally drawn among images (15% of the training set). Random rotations (0 to 180°), shifts (0 to 10mm) and horizontal flips were applied as data augmentation.

2.3 Neural network architecture

Inspired by YOLO [21], we present a single-stage neural network architecture for aneurysm pose estimation in 3D images. As shown in Fig. 2, our architecture follows a grid-based approach and divides the input 3D patch ($96 \times 96 \times 96$ voxels) into $12 \times 12 \times 12 = 1728$ cells of $8 \times 8 \times 8$ voxels.

To encode the input patch into feature maps, we use residual convolutional blocks and down-sampling operations. The *Localization and Orientation Head*

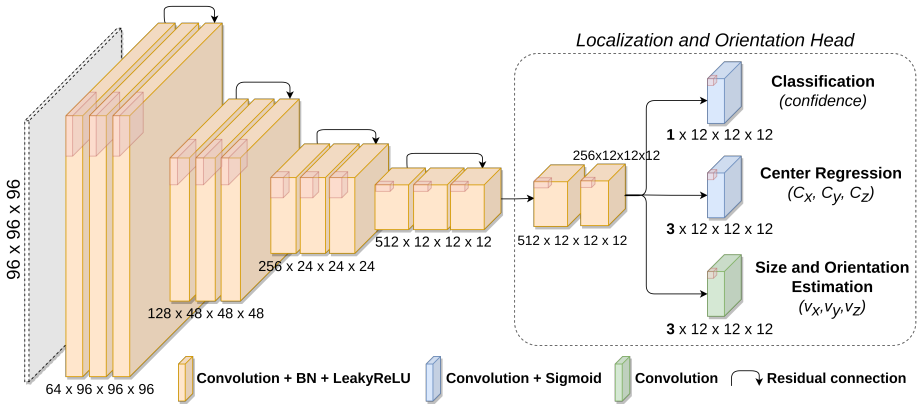

Fig. 2: Our aneurysm pose estimation architecture. 2D feature maps are used only for visualization purposes; their actual sizes in 3D are displayed.

splits the encoded feature maps into a grid of 1728 cells using two consecutive convolutional blocks followed by three parallel convolutions. The first convolution generates a confidence probability score indicating whether the cell contains an aneurysm center. For positive cells (i.e. containing an aneurysm center), the second convolution, followed by sigmoid function, predicts the aneurysm center coordinates $C = (C_x, C_y, C_z)$ relative to the cell size, while the third convolution estimates the aneurysm size and its orientation by calculating the axis vector $\vec{v} = (v_x, v_y, v_z)$. The aneurysm radius is given by $r = |\vec{v}|$, and its orientation by $\vec{v}/|\vec{v}|$. Each prediction can also be represented as a sphere (center C, radius r).

2.4 Loss function

Due to the grid-based nature of our architecture, there is a high imbalance between the number of negative cells and a very small number of positive cells. Inspired by [21], a weighted loss function was employed, which encompasses the sum of terms pertaining to confidence, localization, and orientation estimation.

To optimize the detection confidence, we used the binary cross-entropy (BCE) loss function for both positive (BCE_P) and negative (BCE_N) cells. To prioritize identifying aneurysms over background, we weighted the negative cell term by half the number of positive cells ($\#P$) in the batch (Eq. 1). Aneurysm localization and dimensions are assessed using mean squared error (MSE) (Eq. 2). Orientation estimation is enforced through the cosine similarity of $\vec{v}$ (Eq. 3). These last two terms are only computed on positive cells with a weight of 5 to account for the limited number of such cells.

$$\begin{cases} \text{Confidence} = \text{BCE}_P + 0.5 \times \#P \times \text{BCE}_N & (1) \\ \text{Localization} = 5 \times \text{MSE}(C_x, C_y, C_z, v_x, v_y, v_z) \quad \text{(0 for negative cells)} & (2) \\ \text{Orientation} = 5 \times (1 - \text{Cosine Similarity}(\vec{v})) \quad \text{(0 for negative cells)} & (3) \end{cases}$$

2.5 Implementation details

We implemented our method using PyTorch framework (1.10.0). The model has approximately 28 million parameters, that were optimized using the stochastic gradient descent algorithm. The hyper-parameters were determined using a subset of the in-house dataset: 200 epochs, balanced batch sampling technique between negative and positive patches, batch size of 32, and initial learning rate of 10^{-2}. Each input volume was normalized using z-score normalization. Training and inference were performed on an NVIDIA RTX A6000 GPU with 48 GB of memory.

During inference, a patch reconstruction technique is used to predict the location and orientation of aneurysms in the entire volume. The original volume is split into patches with an isotropic voxel resolution of 0.4mm. To mitigate border effects caused by convolutions, a 16 voxel overlap is considered between adjacent patches. Predictions are made for each patch and converted back to the original volume resolution: a pose is kept only if the predicted center is inside the central $64 \times 64 \times 64$ part of the patch. Non-Maximum Suppression (NMS) is used to eliminate overlapping predictions, considered as spheres (see Section 2.3).

2.6 Evaluation metrics

For the pose estimation task, our method was evaluated based on two standard metrics. First, the Euclidean distance (in mm) was measured between the predicted aneurysm center (C) and its corresponding ground truth (GT). The second metric computes the angular difference (in degrees) between the predicted aneurysm orientation vector ($\vec{v}$) and its corresponding GT.

For the detection task, our evaluation was based on the Intersection-over-Union (IoU) between the predicted and GT spheres at a threshold of 10% [3,16]. A GT sphere with an IoU score above 10% was tagged as a true positive (TP), else it was a false negative (FN). A false positive (FP) was counted for each predicted sphere with no IoU score above 10%. We report the Average Precision metric ($AP_{0.1}$), as well as the sensitivity score ($Sensitivity_{0.5}$) and the number of false positives per case ($FPs/case_{0.5}$), both at a default 50% confidence threshold.

3 Experiments and results

3.1 Pose estimation

We conducted 5-fold cross-validation separately on two large datasets (see Section 2.1) to evaluate the performance of our method for aneurysm pose estimation. Each dataset was randomly split into five subsets, with 25 or 26 patients per subset for the in-house dataset and 54 patients per subset for dataset [7]. The number of aneurysms and mean aneurysm size for each subset were as follows: (In-house) aneurysms: 47, 32, 45, 38, and 44; size: 4.15mm, 3.61mm, 3.88mm, 3.85mm, and 4.25mm; (Dataset [7]) aneurysms: 32, 33, 43, 28, and 28; size: 3.56mm, 3.19mm, 4.05mm, 4.21mm, and 3.70mm. We trained five models

Datasets	Center error (mm)			Orientation error (°)		
	Mean ± std	Median	Range	Mean ± std	Median	Range
In-house	0.54 ± 0.32	0.49	0.05 - 1.74	15.26 ± 10.92	11.91	0.21 - 68.35
Dataset [7]	0.51 ± 0.26	0.48	0.05 - 1.43	14.58 ± 10.53	12.27	1.05 - 68.30

Table 1: Pose estimation performance evaluation of our method.

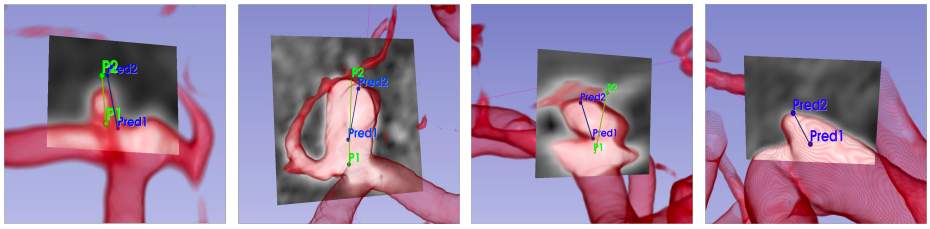

(a) (b) (c) (d)

Fig. 3: Qualitative results on dataset [7]: predicted (blue) and GT (green) landmarks. Each reformatted cut plane was determined by rotating around the aneurysm axis passing through the predicted landmarks. The orientation error is (a) 8.2°, (b) 10.62°, (c) 41.54°, (d) unlabelled aneurysm detected by our method.

for each dataset, using four subsets for training and one subset for testing. This resulted in, for each fold, around 9655 training patches for the in-house dataset and 7595 training patches for dataset [7].

The results on both datasets are shown in Table 1. In the in-house dataset, the median (mean ± std) errors were 0.49mm (0.54mm±0.32) for the aneurysm center location; and 11.91° (15.26°±10.92) for its orientation. In dataset [7], the median errors were 0.48 mm (0.51mm±0.26) for the center location; and 12.27° (14.58°±10.53), for the orientation.

Figure 3 illustrates that the pose computed by our method is sufficiently accurate for clinical use. It was used to display a cut plane through aneurysms with diverse shapes and sizes. Fig. 3a reports on the case of a small aneurysm (size 1.97mm). The pose was estimated with 8.20° orientation error and 0.82mm center location error. This accuracy, especially on the location, makes it possible to infer a cut plane through the aneurysm that is fit for immediate clinical analysis. Similarly, the case of a larger, spherical-shaped aneurysm (size 7.69mm) is shown in Fig. 3b. Our method estimated the pose with an orientation error of 10.62° and center location error of 0.72mm. Larger orientation errors occurred in rare cases like the aneurysm in Fig. 3c (size 3.52mm). We related such errors (here 41.54°) to the complex shape of the aneurysm, that implied annotation uncertainty for the axis orientation. Besides, our method was able to detect some aneurysms that were missed in the initial annotation by radiologists. Fig. 3d shows such an aneurysm detection (size 3.50mm).

Methods	**AP**$_{0.1}$ **(%)**	**Sensitivity**$_{0.5}$ **(%)**	**FPs/case**$_{0.5}$
nnDetection [3]	73.68 ± 6.38	84.76 ± 4.72	0.67 ± 0.12
nnUNet [9]	72.46 ± 4.74	71.95 ± 9.11	0.13 ± 0.06
Ours	76.60 ± 5.24	82.93 ± 5.92	0.44 ± 0.04
Ours (In-house)	82.48 ± 6.66	83.01 ± 6.30	0.34 ± 0.11

Table 2: The results (mean ± std) of aneurysm detection task using dataset [7]. The results of our method on the in-house dataset are added for comparison.

3.2 Object detection

We also evaluated the effectiveness of our method on the classical detection task by comparing it with two public and fully-automated state-of-the-art baselines, nnDetection [3] and nnUNet [9]. nnDetection is based on an improved RetinaNet architecture, which has demonstrated superior performance compared to SSD and Faster RCNN [15]. We used 5-fold cross-validation on the public dataset [7] to guarantee the reproducibility of the results. The 5 models trained in Section 3.1 were used to assess the performance of our method. To ensure a fair comparison, we converted the output of nnDetection and nnUNet to spherical representations. Specifically, for nnDetection, we transformed the predicted 3D bounding boxes into spheres using the largest extent of the box as the sphere diameter. For nnUNet, we fitted one sphere on each connected component from the segmented voxel image. The diameter was computed as the maximum distance between two voxel locations, and the confidence score as the maximum predicted voxel value.

As shown in Table 2, our method exhibited competitive performance compared to the two baselines achieving an $AP_{0.1}$ score of 76.60% (nnDetection: 73.68% and nnUNet: 72.46%). Additionally, our method demonstrated a good trade-off between sensitivity and FP/case, with a $Sensitivity_{0.5}$ score of 82.93% associated with 0.44 $FPs/case_{0.5}$. In comparison, based on Free-response Receiver Operating Characteristic (FROC) curves, nnUNet achieves a maximum sensitivity of 81.90% with a higher FP/case of 1.04, while nnDetection achieves the same sensitivity of 82.93% but with a higher FP/case of 0.51.

4 Conclusion

In this paper, we proposed a novel one-stage deep learning approach for aneurysm pose estimation from TOF-MRA images, which can also be used for the classical detection task. It was evaluated using two large datasets, including a public one [7]. The results demonstrate the effectiveness of our proposed method in both tasks. In the pose estimation task, our method achieved good and similar performance on both datasets, accurately estimating the pose of aneurysms with diverse shapes and sizes. Rare errors in orientation were primarily due to small aneurysms and sometimes complex aneurysm shapes, leading to weak and uncertain GT annotations. Specifically, on the public dataset [7], the median orientation error was 14.79° for small aneurysms (<3mm), 11.49° for medium-sized

aneurysms (3-5mm), and 10.69° for large aneurysms. A current work consists in giving a better clinical definition of the aneurysm axis to reduce this error.

In the aneurysm detection task, our proposed method exhibited promising performance compared to two state-of-the-art baselines, nnDetection [3] and nnUNet [9], with an average precision score of 76.60% and a good balance between sensitivity and FPs/case scores. Besides, these baselines are more computationally demanding compared to our method, which is based on small non-intersecting patches. Out of the 164 aneurysms in dataset [7], half of the 28 FN aneurysms had a size below 3mm. Part of these misses are related to the annotation uncertainty on such aneurysms, which are difficult to diagnose in TOF-MRA [11]. Nevertheless, our future work will address this specific class of aneurysms, including the management of multiple annotators for finer uncertainty modeling.

Our method represents a promising step towards automated aneurysm pose estimation and detection, offering several advantages over existing approaches. It demonstrated multi-task learning capabilities by simultaneously localizing, and estimating the size and the orientation of aneurysms in a single forward pass. Preliminary qualitative tests are hopeful indicators for its clinical utility.

Acknowledgments

The authors would like to acknowledge the financial support provided by the Grand-Est Region and the University Hospital (CHRU) of Nancy, France.

References

1. Arimura, H., Li, Q., Korogi, Y., el al.: Automated computerized scheme for detection of unruptured intracranial aneurysms in three-dimensional magnetic resonance angiography1. Academic radiology **11**(10), 1093–1104 (2004)
2. Assis, Y., Liao, L., Pierre, F., Anxionnat, R., Kerrien, E.: An efficient data strategy for the detection of brain aneurysms from MRA with deep learning. In: Deep Generative Models, and Data Augmentation, Labelling, and Imperfections, pp. 226–234. Springer (2021)
3. Baumgartner, M., Jäger, P.F., Isensee, F., et al.: nnDetection: A self-configuring method for medical object detection. In: International Conference on Medical Image Computing and Computer-Assisted Intervention. pp. 530–539. Springer (2021)
4. Benner, T., Wisco, J.J., van der Kouwe, A.J., Fischl, B., et al.: Comparison of manual and automatic section positioning of brain MR images. Radiology **239**(1), 246–254 (2006)
5. Bystrov, D., Pekar, V., Young, S., Dries, S.P., Heese, H.S., van Muiswinkel, A.M.: Automated planning of MRI scans of knee joints. In: Medical Imaging 2007: Visualization and Image-Guided Procedures. vol. 6509, pp. 1023–1031. SPIE (2007)
6. Çiçek, Ö., Abdulkadir, A., Lienkamp, S.S., et al.: 3D U-Net: learning dense volumetric segmentation from sparse annotation. In: International conference on medical image computing and computer-assisted intervention. pp. 424–432. Springer (2016)

7. Di Noto, T., Marie, G., Tourbier, S., el al.: Towards automated brain aneurysm detection in TOF-MRA: open data, weak labels, and anatomical knowledge. Neuroinformatics pp. 1–14 (2022)
8. Fedorov, A., Beichel, R., Kalpathy-Cramer, J., et al.: 3D Slicer as an image computing platform for the quantitative imaging network. Magnetic resonance imaging **30**(9), 1323–1341 (2012), `https://slicer.org`, pMID: 22770690
9. Isensee, F., Jaeger, P.F., Kohl, S.A., Petersen, J., Maier-Hein, K.H.: nnU-Net: a self-configuring method for deep learning-based biomedical image segmentation. Nature methods **18**(2), 203–211 (2021)
10. Iskurt, A., Becerikli, Y., Mahmutyazicioglu, K.: Automatic identification of landmarks for standard slice positioning in brain mri. Journal of Magnetic Resonance Imaging **34**(3), 499–510 (2011)
11. Jang, M., Kim, J., Park, J., et al.: Features of "false positive" unruptured intracranial aneurysms on screening magnetic resonance angiography. PloS one **15**(9), e0238597 (2020)
12. van der Kouwe, A.J., Benner, T., Fischl, B., Schmitt, F., Salat, D.H., Harder, M., Sorensen, A.G., Dale, A.M.: On-line automatic slice positioning for brain MR imaging. Neuroimage **27**(1), 222–230 (2005)
13. Lall, R., Eddleman, C.S., Bendok, B.R., et al.: Unruptured intracranial aneurysms and the assessment of rupture risk based on anatomical and morphological factors: sifting through the sands of data. Neurosurgical focus **26**(5), E2 (2009)
14. Lecouvet, F.E., Claus, J., Schmitz, P., Denolin, V., Bos, C., Vande Berg, B.C.: Clinical evaluation of automated scan prescription of knee MR images. Journal of Magnetic Resonance Imaging: An Official Journal of the International Society for Magnetic Resonance in Medicine **29**(1), 141–145 (2009)
15. Lin, T.Y., Goyal, P., Girshick, R., He, K., Dollár, P.: Focal loss for dense object detection. In: Proceedings of the IEEE international conference on computer vision. pp. 2980–2988 (2017)
16. Maier-Hein, L., Reinke, A., Christodoulou, E., Glocker, B., Godau, P., Isensee, F., Kleesiek, J., Kozubek, M., Reyes, M., Riegler, M.A., et al.: Metrics reloaded: Pitfalls and recommendations for image analysis validation. arXiv preprint arXiv:2206.01653 (2022)
17. Miao, S., Lucas, J., Liao, R.: Automatic pose initialization for accurate 2D/3D registration applied to abdominal aortic aneurysm endovascular repair. In: Medical Imaging 2012: Image-Guided Procedures, Robotic Interventions, and Modeling. vol. 8316, pp. 243–250. SPIE (2012)
18. Milletari, F., Navab, N., Ahmadi, S.A.: V-net: Fully convolutional neural networks for volumetric medical image segmentation. In: 2016 fourth international conference on 3D vision (3DV). pp. 565–571. Ieee (2016)
19. Nakao, T., Hanaoka, S., Nomura, Y., el al.: Deep neural network-based computer-assisted detection of cerebral aneurysms in MR angiography. Journal of Magnetic Resonance Imaging **47**(4), 948–953 (2018)
20. Reda, F.A., Zhan, Y., Zhou, X.S.: A steering engine: Learning 3-D anatomy orientation using regression forests. In: Medical Image Computing and Computer-Assisted Intervention–MICCAI 2015: 18th International Conference, Munich, Germany, October 5-9, 2015, Proceedings, Part III 18. pp. 612–619. Springer (2015)
21. Redmon, J., Farhadi, A.: Yolov3: An incremental improvement. arXiv preprint arXiv:1804.02767 (2018)
22. Ren, S., He, K., Girshick, R., Sun, J.: Faster R-CNN: Towards real-time object detection with region proposal networks. Advances in neural information processing systems **28** (2015)

23. Sichtermann, T., Faron, A., Sijben, R., et al.: Deep learning–based detection of intracranial aneurysms in 3D TOF-MRA. American Journal of Neuroradiology **40**(1), 25–32 (2019)
24. Stember, J.N., Chang, P., Stember, D.M., et al.: Convolutional neural networks for the detection and measurement of cerebral aneurysms on magnetic resonance angiography. Journal of digital imaging **32**(5), 808–815 (2019)
25. Timmins, K.M., van der Schaaf, I.C., Bennink, E., et al.: Comparing methods of detecting and segmenting unruptured intracranial aneurysms on TOF-MRAs: The ADAM challenge. Neuroimage **238**, 118216 (2021)
26. Ueda, D., Yamamoto, A., Nishimori, M., el al.: Deep learning for MR angiography: automated detection of cerebral aneurysms. Radiology **290**(1), 187–194 (2019)
27. Yang, X., Blezek, D.J., Cheng, L.T., et al.: Computer-aided detection of intracranial aneurysms in MR angiography. Journal of digital imaging **24**(1), 86–95 (2011)
28. Zhan, Y., Dewan, M., Harder, M., Krishnan, A., Zhou, X.S.: Robust automatic knee MR slice positioning through redundant and hierarchical anatomy detection. IEEE transactions on medical imaging **30**(12), 2087–2100 (2011)
29. Zhao, Y., Zeng, K., Zhao, Y., et al.: Deep learning solution for medical image localization and orientation detection. Medical Image Analysis **81**, 102529 (2022)
30. Zhou, Y., Barnes, C., Lu, J., Yang, J., Li, H.: On the continuity of rotation representations in neural networks. In: Proceedings of the IEEE/CVF Conference on Computer Vision and Pattern Recognition. pp. 5745–5753 (2019)